

Interpreting the diversity of afterglow emission from radio-detected tidal disruption events with instantaneous and delayed outflows

Yuri Sato,^{1,*} Mukul Bhattacharya,^{2,3} Jose Carpio,⁴ Jewel Capili,^{5,6} and Kohta Murase^{7,8}

¹ *Astronomical Institute, Graduate School of Science, Tohoku University, Sendai 980-8578, Japan*

² *Department of Physics, Wisconsin IceCube Particle Astrophysics Center, University of Wisconsin, Madison, WI 53703, USA*

³ *Department of Astronomy, Astrophysics and Space Engineering, Indian Institute of Technology Indore, Simrol, MP 453552, India*

⁴ *Department of Physics & Astronomy; Nevada Center for Astrophysics, University of Nevada, Las Vegas, NV 89154, USA*

⁵ *Department of Physics, California Polytechnic State University, San Luis Obispo, CA, 93401, USA*

⁶ *Department of Religious Studies, Naropa University, Boulder, CO, 80302*

⁷ *Department of Physics; Department of Astronomy & Astrophysics; Center for Multimessenger Astrophysics, Institute for Gravitation and the Cosmos, The Pennsylvania State University, University Park, PA 16802, USA*

⁸ *Center for Gravitational Physics and Quantum Information, Yukawa Institute for Theoretical Physics, Kyoto University, Kyoto, Kyoto 606-8502, Japan*

(Dated: December 30, 2025)

Tidal disruption events (TDEs) occur when a star is gravitationally disrupted by the tidal field of a supermassive black hole during a close encounter. Radio emission has recently been detected in TDEs and is commonly attributed to synchrotron radiation from both wind and jetted outflows. However, several TDEs exhibit bright radio flares at late times, which cannot be easily explained if the wind is launched promptly after the stellar disruption. In this study, we model the radio light curves of TDEs with delayed radio flares using three scenarios: an instantaneous wind, a delayed wind, and a delayed relativistic jet. We show that the instantaneous wind model struggles to reproduce delayed radio flare events, indicating the necessity of an additional delayed outflow component. In contrast, the delayed wind model provides a consistent explanation for the observed radio phenomenology, successfully reproducing events both with and without delayed radio flares. For some delayed radio flare events (e.g., ASASSN-15oi and AT 2019dsg), both the delayed wind and delayed jet models can reproduce the observed radio light curves. The delayed jet model produces x-ray and optical emission that is detectable at typical TDE distances, in contrast to wind-driven scenarios. This highlights how multiwavelength observations offer an effective means of distinguishing among possible outflow mechanisms.

I. INTRODUCTION

A tidal disruption event (TDE) occurs when a star is torn apart by the tidal forces of a supermassive black hole (SMBH) during a close encounter [1–3]. The stellar debris is divided into roughly equal components: one portion becomes unbound and is ejected into space, while the remainder returns toward the SMBH to form an accretion flow. This process can give rise to multiwavelength emission in radio, infrared (IR)/optical/ultraviolet (UV), x-ray and gamma-ray bands. While the observed thermal emission is commonly interpreted as reprocessed radiation arising from the accreting stellar debris [4–9], the details of the emission mechanism remain uncertain. In addition, nonthermal emission components have been detected in some TDEs, particularly those associated with outflows. Radio emission in such cases is attributed to synchrotron radiation from relativistic electrons accelerated in shocks formed as jets or winds interact with the circumnuclear medium (CNM) (see e.g. Ref. [10]). Future multiwavelength observations are expected to pro-

vide crucial insights into the structure, energetics, and evolution of these outflows [10–12].

Some TDEs, such as Swift J1644+57 [13, 14], Swift J2058+05 [15], Swift J1112-8238 [16], and AT2022cmc [17], exhibit radio luminosities exceeding 10^{40} erg s $^{-1}$ and are widely interpreted as jetted TDEs, involving the launch of relativistic jets (e.g. Ref. [18–22]). In contrast, TDEs with lower peak radio luminosities of $\lesssim 10^{38}$ – 10^{39} erg s $^{-1}$ are generally attributed to sub-relativistic winds and are classified as non-jetted TDEs (see, e.g., Refs. [23–26]). Recently, however, some TDEs have been detected that exhibit radio flares peaking at late times (“delayed radio flare”), around $\sim 10^8$ s after their optical discovery, with peak luminosities of $\sim 10^{38}$ – 10^{39} erg s $^{-1}$ [27–30]. Some of these delayed radio flares are preceded by another, earlier radio flare (“re-brightening radio events”). These events are fainter than jetted TDEs, yet brighter than the typical non-jetted population at a few months. The origin of such delayed radio flares remains unclear.

Several models have been proposed to explain these delayed radio flares. One possibility is the delayed launch of an outflow, either as a spherical wind or a collimated relativistic jet, which interacts with the CNM at late times [29, 31–36]. Another possibility is outflow interaction

* yuri@astr.tohoku.ac.jp (YS)

with a stratified CNM, where the ambient density remains low initially but increases sharply at $\sim 0.1 - 1$ pc, triggering strong radio emission once the outflow reaches this denser region [37–39]. A third scenario involves a transition in the CNM density profile, from a power-law profile to a constant density medium beyond the Bondi radius [40]. Finally, delayed radio brightening may also result from an off-axis relativistic jet. A one-component version of this scenario has been proposed by Ref. [41], while a two-component off-axis jet model has been suggested by Ref. [42], in which a narrow fast jet and a wider slower component contribute to the observed radio brightening. However, distinguishing among these possibilities remains challenging due to insufficient multiwavelength coverage during the late-time evolution of these TDEs [43, 44].

In this paper, we investigate whether the radio emission observed in delayed radio flare TDEs can be consistently explained by delayed outflow models. We consider three scenarios: an instantaneous wind, a delayed wind, and a delayed relativistic jet. To distinguish between these models, we examine the detectability of multiwavelength afterglow emission with the Cherenkov Telescope Array Observatory (CTAO) [45], the *Chandra* X-ray Observatory (*Chandra*) [46], the Vera C. Rubin Observatory (Rubin) [47], the Zwicky Transient Facility (ZTF) [48], the Atacama Large Millimeter/submillimeter Array (ALMA) [49], the Square Kilometre Array (SKA) [50], the Very Large Array (VLA) [51], and the MeerKAT radio telescope (MeerKAT) [52]. In particular, we assess whether x-ray and optical follow-up observations can help break the degeneracy between the models, which often produce similar radio light curves. By comparing model predictions with existing and forthcoming observations, we aim to constrain the physical origin of delayed radio flares and improve our understanding of outflow launch mechanisms in TDEs. This paper is organized as follows. In Section II, we describe our modeling framework for the instantaneous wind, delayed wind, and delayed jet scenarios. In Section III, we compare the model predictions with observed radio light curves for a sample of TDEs exhibiting late-time radio emission. In Section IV, we discuss the prospects of detecting associated multiwavelength (x-ray, optical, radio) afterglows with current and future facilities. Section V is devoted to a discussion of the main results, and the conclusions are presented in Section VI.

II. MODEL DESCRIPTION

In this section, we describe three models – the instantaneous wind, delayed wind, and delayed jet – used to study the outflow dynamics and the associated synchrotron emission. To compute the resulting radio light curves, we utilize the blast wave module of AMES (Astrophysical Multimessenger Emission Simulator), following the methodology described in Refs. [53, 54] (see also

Refs. [42, 55, 56]).

A. Instantaneous wind model

We model the dynamical evolution of a spherical nonrelativistic outflow characterized by an isotropic-equivalent kinetic energy $\mathcal{E}_k^{\text{iso}}$ and an initial velocity v_0 . The outflow propagates into the CNM described by a power-law density profile, $n(R) = AR^{-w} = n_{\text{ext}}(R/10^{18} \text{ cm})^{-w}$ (see Fig. 1 for a schematic picture). We assume that the emission originates from a region at radius R . The evolution of the outflow radius and velocity is given by

$$R = \left(\frac{5-w}{2}\right)^{\frac{2}{5-w}} \left(\frac{(3-w)\mathcal{E}_k^{\text{iso}}}{2\pi Am_p}\right)^{\frac{1}{5-w}} T^{\frac{2}{5-w}}, \quad (1)$$

$$v = \left(\frac{5-w}{2}\right)^{\frac{w-3}{5-w}} \left(\frac{(3-w)\mathcal{E}_k^{\text{iso}}}{2\pi Am_p}\right)^{\frac{1}{5-w}} T^{\frac{w-3}{5-w}}, \quad (2)$$

where v is the outflow velocity, m_p is the proton mass, and $T = t - t_0$ is the observer time measured from the time of optical discovery (t_0), at which the tidal disruption occurs and the outflow is assumed to be launched (see e.g., Refs. [57–59]). As the outflow interacts with the dense external medium, synchrotron and synchrotron self-Compton (SSC) emission is generated. We adopt a power-law energy distribution for the accelerated electrons with index s , and assume constant microphysical parameters ϵ_B , ϵ_e , and f_e , which represent the fractions of internal energy transferred to magnetic fields, nonthermal electrons, and the fraction of accelerated electrons, respectively. The downstream magnetic field, amplified by shocks, is estimated as (e.g., Ref. [60, 61])

$$B' = (8\pi\epsilon_B m_p n(R)v^2)^{1/2}. \quad (3)$$

The minimum Lorentz factor of accelerated electrons is

$$\gamma_m \simeq \frac{\epsilon_e}{f_e} \left(\frac{s-2}{s-1}\right) \frac{m_p}{m_e} \frac{v^2}{c^2}. \quad (4)$$

The corresponding minimum synchrotron frequency is

$$\nu_m \approx (1.6 \times 10^{14} \text{ Hz}) \frac{1}{1+z} \left(\frac{s-2}{s-1}\right)^2 \mathcal{E}_{52}^{\frac{10-w}{2(5-w)}} n_{-1}^{-\frac{2w+1}{2(5-w)}} \times \epsilon_{B,-2}^{1/2} \epsilon_{e,-1}^2 f_{e,0}^{-2} T_5^{\frac{4w-15}{5-w}}, \quad (5)$$

where z is the redshift, $\mathcal{E}_{52} = \mathcal{E}_k^{\text{iso}}/10^{52} \text{ erg}$, $n_{-1} = n_{\text{ext}}/10^{-1} \text{ cm}^{-3}$, $\epsilon_{B,-2} = \epsilon_B/10^{-2}$, $\epsilon_{e,-1} = \epsilon_e/10^{-1}$, $f_{e,0} = f_e/1.0$, and $T_5 = T/10^5 \text{ s}$. The synchrotron cooling frequency is given by

$$\nu_c \approx (1.7 \times 10^{15} \text{ Hz}) \frac{1}{1+z} \mathcal{E}_{52}^{-\frac{3(2-w)}{2(5-w)}} n_{-1}^{-\frac{3(7-2w)}{2(5-w)}} \epsilon_{B,-2}^{-3/2} T_5^{\frac{2w-1}{5-w}}. \quad (6)$$

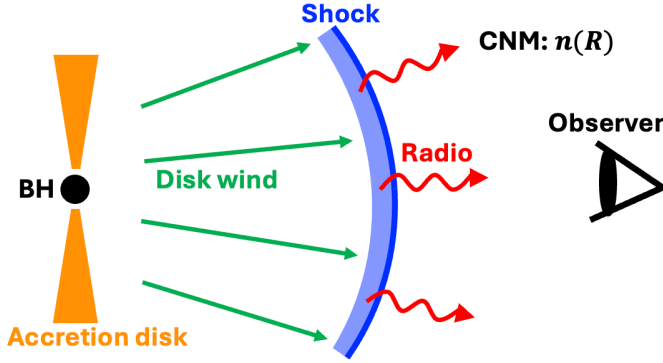


FIG. 1. Schematic illustration of the instantaneous wind model. A nonrelativistic wind is launched from the accretion disk after the stellar disruption. The wind drives a forward shock into the CNM with a power-law density profile, $n(R)$, producing synchrotron emission from shock-accelerated electrons.

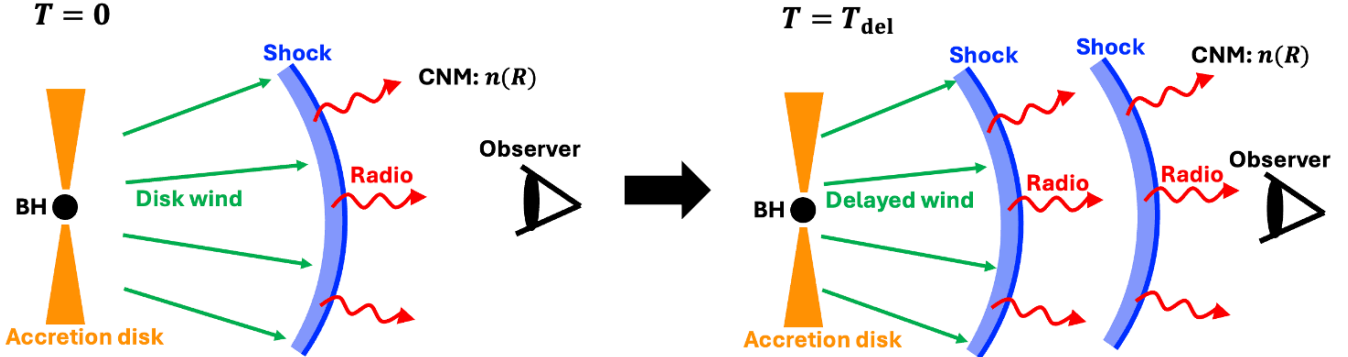


FIG. 2. Schematic illustration of the delayed wind model. At $T = 0$, the initial nonrelativistic wind is launched from the accretion disk. Subsequently, a second wind component is launched at a time delay $T = T_{\text{del}}$, following the initial wind. Similar to the initial nonrelativistic wind, the delayed wind also interacts with the CNM, driving a shock that produces renewed synchrotron emission.

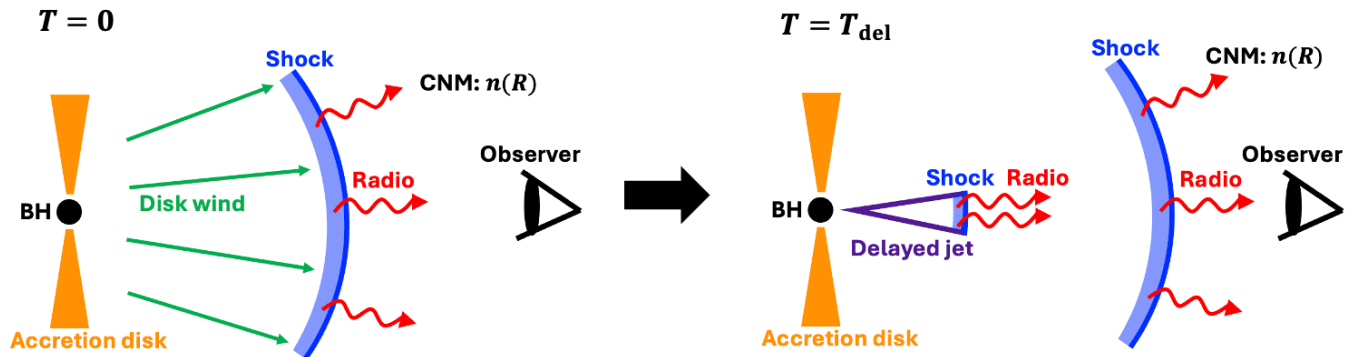


FIG. 3. Schematic illustration of the delayed jet model. At $T = 0$, the initial nonrelativistic wind is launched from the accretion disk. Subsequently, at $T = T_{\text{del}}$, a relativistic jet is launched. The jet propagates into the CNM, driving a forward shock that forms a thin shell. Synchrotron radiation is emitted from this shocked region as the jet decelerates and evolves.

Synchrotron self-absorption suppresses radio emission at low frequencies. The synchrotron self-absorption frequency ν_a is defined by the condition $\tau_{\text{ssa}}(\nu_a) = 1$, where τ_{ssa} is the corresponding optical depth.

As the observed radio spectra of most TDEs exhibit the frequency ordering $\nu_m < \nu_a < \nu_c$ at late times (see, e.g., Ref. [29]), we adopt the same spectral regime to compute the synchrotron self-absorption frequency:

$$\nu_a \approx (6.9 \times 10^{10} \text{ Hz}) \frac{1}{1+z} \left(\frac{s-2}{s-1} \right)^{\frac{2(s-1)}{s+4}} \mathcal{E}_{52}^{\frac{10s-(s+6)w}{2(5-w)(s+4)}} \times n_{-1}^{\frac{(18-s)-2sw}{2(5-w)(s+4)}} \epsilon_{B,-2}^{\frac{s+1}{2(s+4)}} \epsilon_{e,-1}^{\frac{2(s-1)}{s+4}} f_{e,0}^{\frac{2(1-s)}{s+4}} T_5^{\frac{4(s-2)w+5(2-3s)}{(5-w)(s+4)}}. \quad (7)$$

The synchrotron peak flux is given by

$$F_{\nu}^{\text{max}} \approx (5.3 \times 10^5 \text{ mJy}) \frac{(1+z)}{d_{L,28}^2} \mathcal{E}_{52}^{\frac{8-3w}{2(5-w)}} n_{-1}^{\frac{2w+11}{2(5-w)}} \epsilon_{B,-2}^{1/2} f_{e,0} T_5^{\frac{3-2w}{5-w}} \quad (8)$$

where $d_L = d_{L,28} \times 10^{28} \text{ cm}$ is the luminosity distance. The synchrotron spectrum in the regime $\nu_m < \nu_a < \nu_c$ takes the form

$$F_{\nu} = F_{\nu}^{\text{max}} \begin{cases} \left(\frac{\nu}{\nu_m} \right)^2 \left(\frac{\nu_a}{\nu_m} \right)^{-s/2-2}, & \nu \leq \nu_m, \\ \left(\frac{\nu}{\nu_a} \right)^{5/2} \left(\frac{\nu_a}{\nu_m} \right)^{-(s-1)/2}, & \nu_m < \nu \leq \nu_a, \\ \left(\frac{\nu}{\nu_m} \right)^{-(s-1)/2}, & \nu_a < \nu \leq \nu_c, \\ \left(\frac{\nu}{\nu_c} \right)^{-s/2} \left(\frac{\nu_c}{\nu_m} \right)^{-(s-1)/2}, & \nu_c < \nu. \end{cases} \quad (9)$$

Under the condition $\nu_m \leq \nu \leq \nu_a \leq \nu_c$, substituting ν_m , ν_a , and F_{ν}^{max} into Eq. 9 yields the observed flux as a function of time:

$$F_{\nu}(T) \sim (6.5 \times 10^2 \text{ mJy}) \mathcal{E}_{52}^{\frac{(s+3)w+6}{4(5-w)}} n_{-1}^{\frac{6w+5}{4(5-w)}} \epsilon_{B,-2}^{\frac{6-w}{4(5-w)}} f_{e,0} \nu_9^{5/2} T_5^{\frac{11}{4(5-w)}}, \quad (10)$$

where $\nu_9 = \nu/10^9 \text{ Hz}$. In this regime, the light curve peaks when the synchrotron self-absorption frequency ν_a crosses the observing frequency. After the peak, the flux decays as $F_{\nu} \propto T^{-([(s-2)4w+3(7-5s)]/2(5-w)}}$.

B. Delayed wind model

In this model, the second delayed outflow is launched from the accretion disk at a delay time T_{del} following the initial nonrelativistic outflow (see Fig. 2). This delayed wind, characterized by an isotropic kinetic energy $\mathcal{E}_k^{\text{iso}}$ and an initial velocity v_0 , interacts with the CNM, giving rise to renewed synchrotron emission from shock-accelerated electrons. The electron energy distribution is assumed to follow a power-law with index s , and the emission is characterized by microphysical parameters ϵ_e , ϵ_B , and f_e . The outflow dynamics and synchrotron radiation are modeled in the same manner as in Section II A, but with a shifted time origin.

The delayed onset compresses the emission duration in the observer time frame, resulting in a more rapid flux rise shortly after the launch of the delayed outflow. Furthermore, the temporal evolution of the synchrotron break frequencies (ν_a , ν_m , and ν_c) and the flux normalization is governed by the shifted time coordinate $T - T_{\text{del}}$.

As a result, simple analytical power-law scalings in the observer time T are generally not applicable. Nevertheless, similar to the instantaneous wind case, the light curve is still expected to peak when the synchrotron self-absorption frequency ν_a passes through the observing band.

C. Delayed jet model

In the delayed jet model, we assume that a relativistic jet is launched from the SMBH at a delay time T_{del} , following the initial nonrelativistic wind as shown in Fig. 3. The jet propagates into the CNM with a density profile $n(R) = n_{\text{ext}}(R/10^{18} \text{ cm})^{-w}$ and is modeled as a top-hat jet with isotropic-equivalent kinetic energy $\mathcal{E}_k^{\text{iso}}$, initial bulk Lorentz factor Γ_0 , and initial half-opening angle θ_0 . As the jet expands, it drives a forward shock into the CNM, forming a thin shell that produces synchrotron emission. The radiative treatment follows the same prescription as discussed in Section II A. We assume an on-axis observer for our analysis.

As with the delayed wind model, the time shift due to T_{del} compresses the light curve in the observer time frame, making simple power-law approximations with T generally invalid. However, the light curve is still expected to peak when the synchrotron self-absorption frequency ν_a crosses the observing frequency.

III. COMPARISON OF THEORETICAL MODELS WITH OBSERVATIONS

We model the radio light curves of TDEs using three scenarios: (i) an instantaneous wind model, (ii) a delayed wind model, and (iii) a delayed jet model. Our sample consists of 9 TDEs with well-sampled radio light curves, namely ASASSN-14ae, ASASSN-15oi, PS16dmt, iPTF16fnl, ASASSN-19bt, AT 2019dsg, AT 2019ehz, AT 2019eve, and AT 2020vwl. Several events in our sample overlap with those analyzed by Ref. [36].

We classify an event as a delayed radio flare if its peak radio luminosity exceeds $5 \times 10^{37} \text{ erg s}^{-1}$ at $T > 5 \times 10^6 \text{ s}$. Based on this criterion, eight events (all apart from iPTF16fnl) are classified as delayed radio flares. A summary of references reporting radio observations for these sources is provided in Table II. To compute the radio light curves, we utilize the AMES code (see Section II). AMES incorporates key physical processes, including outflow dynamics, synchrotron radiation mechanisms and absorption processes. The typical parameter ranges explored in our analysis are as follows: $n_{\text{ext}} \sim 10^{-10^3} \text{ cm}^{-3}$, $w \sim 1-2$, $s \sim 2.1-2.8$, $\epsilon_B \sim 10^{-4}-10^{-2}$, $\epsilon_e \sim 10^{-2}-0.1$, and $f_e \sim 0.1$. For the wind component, we adopt $v_0 \sim 0.1c$ and $\mathcal{E}_k^{\text{iso}} \sim 5 \times 10^{51} - 5 \times 10^{52} \text{ erg}$. For the relativistic jet component, we assume $\Gamma_0 \sim 3$, $\theta_0 \sim 0.35 \text{ rad}$, and $\mathcal{E}_k^{\text{iso}} \sim 5 \times 10^{52} \text{ erg}$. The launch time of the delayed components is set to $T_{\text{del}} \sim 10^7-10^8 \text{ s}$.

TABLE I. Model fit summary for TDEs with detected radio emission

TDE Name	Two outflows ^a	Instantaneous wind	Delayed wind ^b	Delayed jet ^c
ASASSN-14ae ^d	Yes	✗	✓	✓
ASASSN-15oi ^{d,f}	Yes	✗	✓	✓
PS16dtm ^d	Yes	✗	✓	✓
iPTF16fnl ^e		✓	✓	✗
ASASSN-19bt ^{d,f}	Yes	✗	✓	✗
AT 2019dsg ^{d,f}	Yes	✗	✓	✓
AT 2019ehz ^d		✓	✓	✓
AT 2019eve ^d		✓	✓	✓
AT 2020vwl ^{d,f}	Yes	✗	✓	✗

Notes.^a Two separate outflows (instantaneous wind+delayed wind and/or instantaneous wind+delayed jet).^b Instantaneous wind+delayed wind.^c Instantaneous wind+delayed jet.^d Delayed radio flare event.^e Radio event without a delayed flare.^f Rebrightening radio event.

TABLE II. References for the observed data are listed.

Events	Frequencies	references
ASASSN-14ae	5, 7, and 11 GHz	Ref. [29]
ASASSN-15oi	3, 5, and 23 GHz	Refs. [27, 62, 63]
PS16dtm	3, 6, and 11 GHz	Ref. [29]
iPTF16fnl	5, 7, and 15.5 GHz	Refs. [29, 64]
ASASSN-19bt	2.1, 9, and 17 GHz	Ref. [30]
AT 2019dsg	1.36, 7, and 17 GHz	Refs. [25, 29]
AT 2019ehz	3.5, 9, and 20 GHz	Ref. [29]
AT 2019eve	3.5, 5, and 9 GHz	Ref. [29]
AT 2020vwl	1.25, 5.5, and 9 GHz	Refs. [32, 65]

The best-fit radio light curves are shown in Figures 4, 5, and 6, and Table I, with the best-fit model parameters summarized in Table III.

A. TDEs with delayed radio flares

For the following events, the instantaneous wind scenario fails to explain the late-time rise in the radio flux, as it predicts a monotonic decline once the absorption frequency ν_a passes through the radio bands (see Sec. II A). Instead, the delayed wind and/or delayed jet models, in which the outflow is launched at $T_{\text{del}} \sim 10^7\text{--}10^8$ s, can account for the delayed radio brightening observed in these events:

ASASSN-14ae, *ASASSN-15oi*, *PS16dtm*, & *AT 2019dsg*. In the instantaneous wind model, the radio flux decays after ν_a crosses the observational band, which is inconsistent with the observed late-time rise.

A delayed wind or jet scenario, where the outflow is launched after a significant time lag ($T_{\text{del}} \sim 10^7\text{--}10^8$ s), can explain the delayed peak in the radio light curve. For PS16dtm, the light curve in the delayed jet scenario exhibits two distinct peaks. The first peak corresponds to the deceleration time of the jet, while the second arises when the synchrotron self-absorption frequency crosses the observing frequency.

ASASSN-19bt & *AT 2020vwl*. Similar to ASASSN-15oi and AT 2019dsg, these two events exhibit detectable radio emission not only at early times but also at late times ($\sim 10^8$ s). In particular, AT2020vwl displays re-brightening in its radio light curve. Delayed radio re-brightening is difficult to reconcile with a single outflow component and instead suggests the presence of an additional delayed outflow. The late-time radio emission in these events is consistent with the delayed wind model, whereas the delayed jet scenario is disfavored. This is because, in the Blandford–McKee phase, the relativistic shock decelerates rapidly ($R \propto T^{1/(4-w)}$, $\Gamma \propto T^{(w-3)/2(4-w)}$), leading to a sharp post-peak decline in emission. In contrast, a Newtonian outflow decelerates more gradually ($v \propto T^{(w-3)/(5-w)}$), producing a slower flux decay, consistent with the observed light curves.

AT 2019ehz & *AT 2019eve*. The observed radio light curve can be explained by either an instantaneous wind or a delayed outflow (wind or jet). In these cases, the introduction of a delayed component is not strictly necessary. For AT 2019eve, the light curve in the delayed jet scenario exhibits two distinct peaks. While the first peak corresponds to the deceleration time of the jet, the second emerges when the synchrotron self-absorption frequency drops below the observing frequency, similar to the behavior observed in PS16dtm.

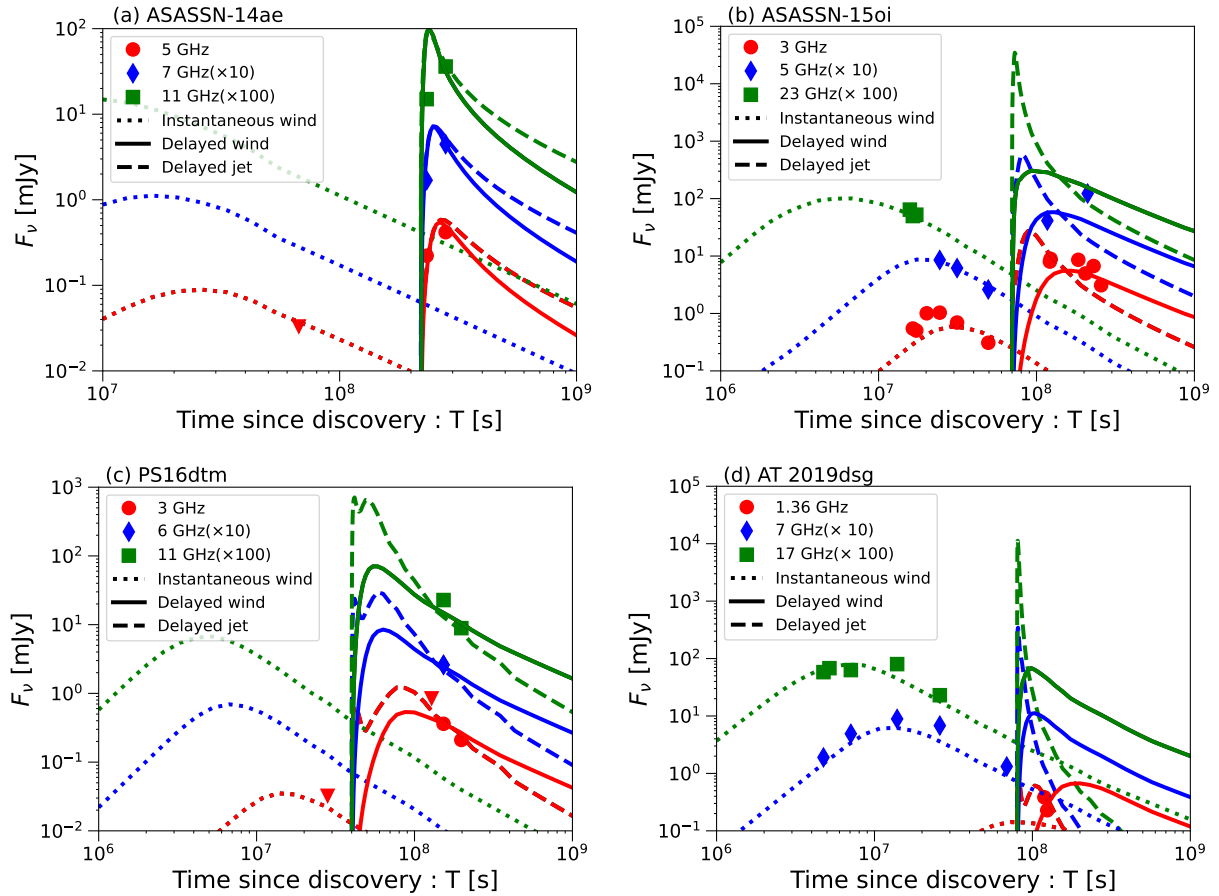


FIG. 4. Observed radio data for ASASSN-14ae in panel (a), ASASSN-15oi in panel (b), PS16dtm in panel (c), and AT 2019dsg in panel (d) are shown (see plot legends for frequencies corresponding to radio observations considered). These are compared with the radio light curves calculated from our theoretical models. In each panel, the dotted, solid, and dashed lines represent the emission from the instantaneous wind, delayed wind and delayed jet, respectively. The upper limits in radio flux are shown with downward triangles. For these four events, the observed radio data suggests the presence of delayed outflows, either in the form of a jet or a wind.

B. DEs without delayed radio flares

iPTF16fnl. Both the instantaneous wind and delayed wind models can reproduce the late-time radio data. Note that the inferred isotropic kinetic energy using the delayed wind model is lower than that of the delayed flare TDEs. This is because iPTF16fnl is the only event in our sample classified as exhibiting a TDE without delayed radio flare, whose peak radio luminosity is lower than that of the events with delayed flares. In contrast, the delayed jet model predicts a rapid decline after the peak, which is inconsistent with the observed radio light curve. As in ASASSN-19bt and AT 2020vwl, this arises due to deceleration of the relativistic jet, which causes a steep decline in radio emission as the relativistic beaming reduces. In contrast, emission from the nonrelativistic wind decays more gradually, as the outflow remains in the Newtonian regime. Given that the instantaneous wind model requires fewer model parameters compared to the delayed wind or jet scenarios, it is favored as a

natural explanation for this event.

IV. TESTING MODELS WITH MULTIWAVELENGTH OBSERVATIONS

In Sec. III, we found that some events can be explained by both the delayed wind and delayed jet models. Therefore, it is challenging to distinguish between these scenarios solely based on radio observations. In this section, we investigate whether multiwavelength observations using TeV gamma-ray (CTAO), x-ray (*Chandra*), optical (Rubin, ZTF), and radio (ALMA, SKA, VLA, MeerKAT) facilities can serve as diagnostics to discriminate among the instantaneous wind, delayed wind, and delayed jet models.

To this end, we compute both the synchrotron and SSC emission for each model using the following parameter sets. For the instantaneous wind model, we adopt $\mathcal{E}_k^{\text{iso}} = 5.0 \times 10^{51}$ erg, $v_0 = 0.1c$, and $T_{\text{del}} = 0$ s. For the de-

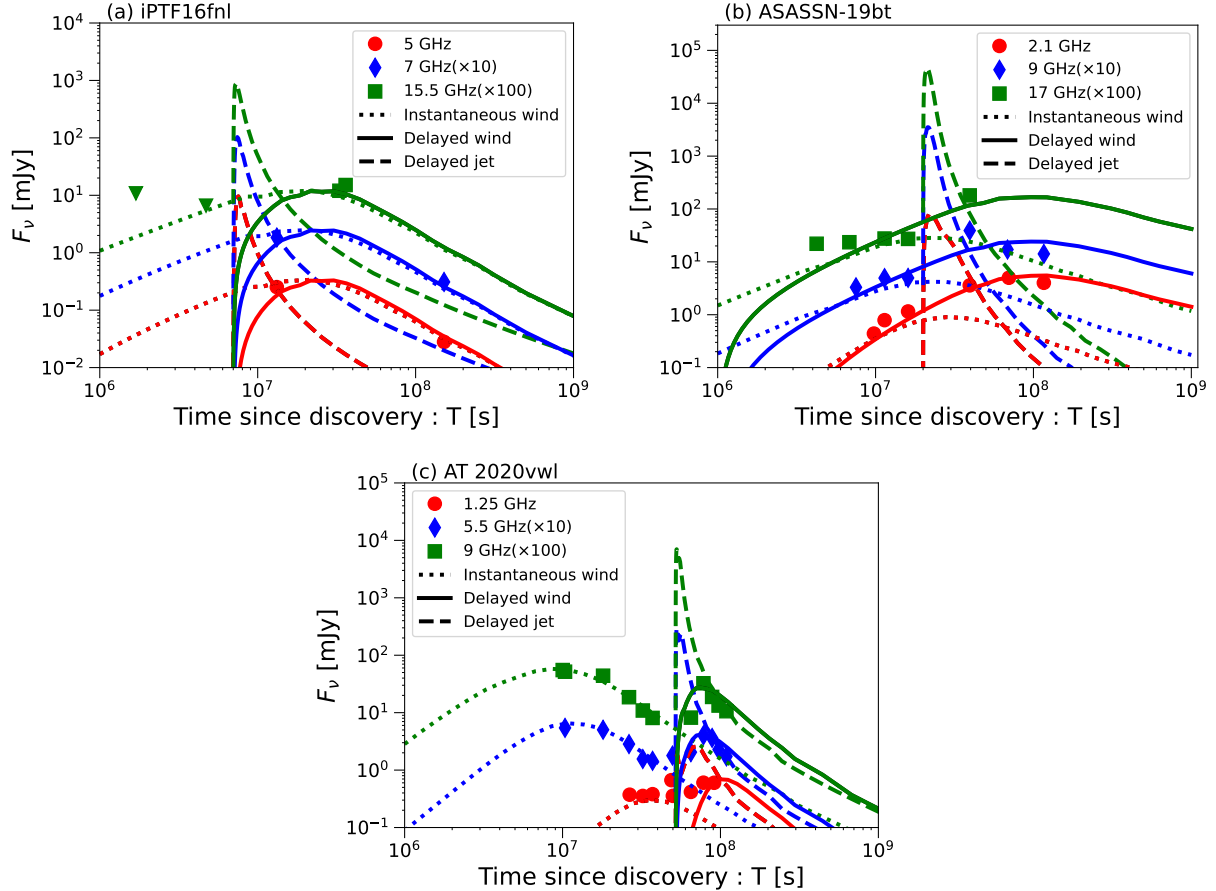


FIG. 5. Observed radio data for iPTF16fnl in panel (a), ASASSN-19bt in panel (b), and AT 2020vwl in panel (c) are shown (see plot legends for frequencies corresponding to radio observations considered). The radio observations are compared with the predictions of our theoretical models. The line types and downward triangles shown here have the same meaning as in Figure 4. For these three events, the radio emission from a delayed jet is inconsistent with the observed radio flux.

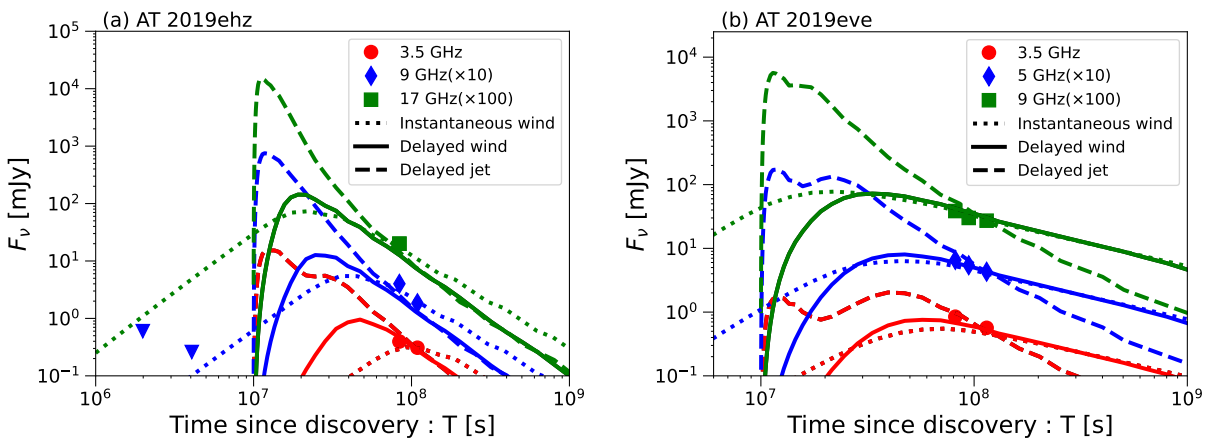


FIG. 6. Observed radio data for AT 2019ehz in panel (a) and AT 2019eve in panel (b) are shown (see plot legends for corresponding observing frequencies). Radio observations are compared with light curves inferred from the three theoretical models. The line types and downward triangles have the same meaning as in Figure 4. For these events, all three models – instantaneous wind, delayed wind, and delayed jet – can explain the observed radio data.

layered wind model, we use $\mathcal{E}_k^{\text{iso}} = 5.0 \times 10^{52}$ erg, $v_0 = 0.1c$, and $T_{\text{del}} = 1.0 \times 10^8$ s. For the delayed jet model, we adopt $\theta_v = 0$, $\theta_0 = 0.35$ rad, $\mathcal{E}_k^{\text{iso}} = 5.0 \times 10^{52}$ erg, $\Gamma_0 = 3$, and $T_{\text{del}} = 1.0 \times 10^8$ s. In all cases, we fix the external-medium and microphysical parameters to $n_{\text{ext}} = 10^3 \text{ cm}^{-3}$, $w = 1.0$, $s = 2.4$, $\epsilon_B = 0.01$, $\epsilon_e = 0.1$, and $f_e = 0.1$. We assume a redshift of $z = 0.014$ ($d_L = 60$ Mpc), representative of nearby optical TDEs such as iPTF16fnl and more recent events including AT 2025aarm [66].

We present the results in Fig. 7. The x-ray telescope *Chandra* and the optical telescope Rubin have the potential to detect the emission from the delayed jet. In contrast, x-ray and optical afterglows from the instantaneous wind and delayed wind models are challenging to detect with *Chandra* and Rubin. This is because the emission from the relativistic jet is significantly brighter than that from the nonrelativistic outflows due to Doppler beaming. The x-ray and optical observations could therefore reveal key outflow properties, such as the launch time and velocity, for radio-detected TDEs. Detection with ZTF is expected to be difficult in all model scenarios. TeV gamma-ray emission is too faint to be detected with CTAO in any of the models, as the SSC component remains well below the CTAO sensitivity.

At radio frequencies, all three models are potentially detectable at low frequencies, such as those observed with MeerKAT or VLA. However, only the emission from the delayed jet model exceeds the sensitivity threshold in the high-frequency regime accessible by ALMA. Although ALMA's sensitivity decreases toward higher frequencies, the delayed jet remains in a transrelativistic phase at $\sim 10^8$ s. In contrast, both the instantaneous and delayed wind models have already entered the nonrelativistic phase by that time, resulting in significantly lower fluxes. As a result, the delayed jet produces the highest flux among the models at these high frequencies, making it detectable by ALMA, despite its more limited sensitivity in this regime.

V. DISCUSSION

As shown in Table I, for the delayed radio flare TDEs, the isotropic kinetic energy inferred for the delayed wind and delayed jet components is an order of magnitude larger than that of the instantaneous wind. This trend may reflect the fact that the late-time ($\gtrsim 10^8$ s) radio emission is brighter than the early-time emission ($\lesssim 10^8$ s), requiring a more energetic outflow to explain the observed flux. However, the physical mechanisms responsible for launching such powerful outflows at delayed times remain uncertain. Several possibilities have been proposed to explain the delayed launching of outflows in TDEs. These include a time lag in the formation of an accretion disk due to inefficient circularization of stellar debris [67] or the disk transition due to the change of the accretion rate [68], delayed jet launch resulting from the

gradual accumulation of magnetic flux and the eventual activation of the Blandford–Znajek mechanism [69], and episodic reactivation of accretion driven outflows by fallback rate fluctuations [70]. Such delayed processes may allow the subsequent production of more massive and energetic outflows, than what would be expected from prompt ejection. In contrast, the TDE iPTF16fnl, which does not exhibit a delayed radio flare, shows an isotropic kinetic energy for the delayed wind component that is comparable to that inferred for the instantaneous wind. This is because iPTF16fnl has a peak radio luminosity of $\sim 10^{37}$ erg s $^{-1}$, which is about two orders of magnitude dimmer than that of the delayed radio flare TDEs. This suggests that outflows launched promptly after disruption may be intrinsically less energetic.

Radio rebrightening events in our sample appear to require the presence of two distinct outflow components, either in the form of two winds or a combination of a wind and a jet (see Table I). Nevertheless, even for TDEs that exhibit pronounced late-time radio flares, such as AT 2019ehz and AT 2019eve, the inclusion of a delayed outflow component is not strictly necessary to reproduce the observed light curves (see Table I and Fig. 6). This diversity in radio behavior likely reflects underlying differences in the physical properties of the accretion disk, such as the efficiency of debris circularization, the timescale for disk formation, or the ability to accumulate magnetic flux – which may in turn regulate whether additional outflows are produced and at what epoch they are launched.

The fallback time of the most tightly bound debris can be estimated as $T_{\text{fb}} \sim 10^6$ s $(M_{\text{BH}}/10^7 M_{\odot})^{1/2} (M_*/M_{\odot})^{-1} (R_*/R_{\odot})^{3/2}$, where M_{BH} is the BH mass and M_*/R_* denote the mass/radius of the disrupted star, respectively [2]. By contrast, the inferred delay times for launching outflows are $T_{\text{del}} \sim 10^{7-8}$ s (see Table III), which are at least an order of magnitude longer than T_{fb} . Since the mass fallback rate monotonically declines as $\dot{M}_{\text{fb}} \propto T^{-5/3}$ for $T \gtrsim T_{\text{fb}}$ [2], fallback-driven accretion alone cannot account for the observed late-time radio brightening. This discrepancy motivates the consideration of additional delayed processes capable of powering energetic outflows at late times, such as inefficient debris circularization, gradual accumulation of magnetic flux leading to the activation of a Blandford–Znajek jet, or episodic reactivation of accretion triggered by fluctuations in the fallback rate.

The Bondi radius is estimated to be $r_{\text{B}} \simeq 10^{22} (M_{\text{BH}}/10^7 M_{\odot}) (T_{\text{eff}}/10^4 \text{ K})^{-1} (\gamma/1.67)^{-1} (\mu/0.6) \text{ cm}$, where T_{eff} , γ , and μ are the temperature, adiabatic index, and mean molecular weight of the interstellar medium, respectively [71]. In our calculations, the shock radius remains well within 10^{22} cm before $t \sim 10^9$ s. Therefore, the ambient density can be self-consistently approximated by a single power-law profile, $n(R) \propto R^{-w}$. In contrast, Ref. [40] adopts a much higher interstellar medium temperature, $T_{\text{eff}} \sim 10^7$ K, which reduces the Bondi radius to $r_{\text{B}} \sim 10^{17}$ cm. As a

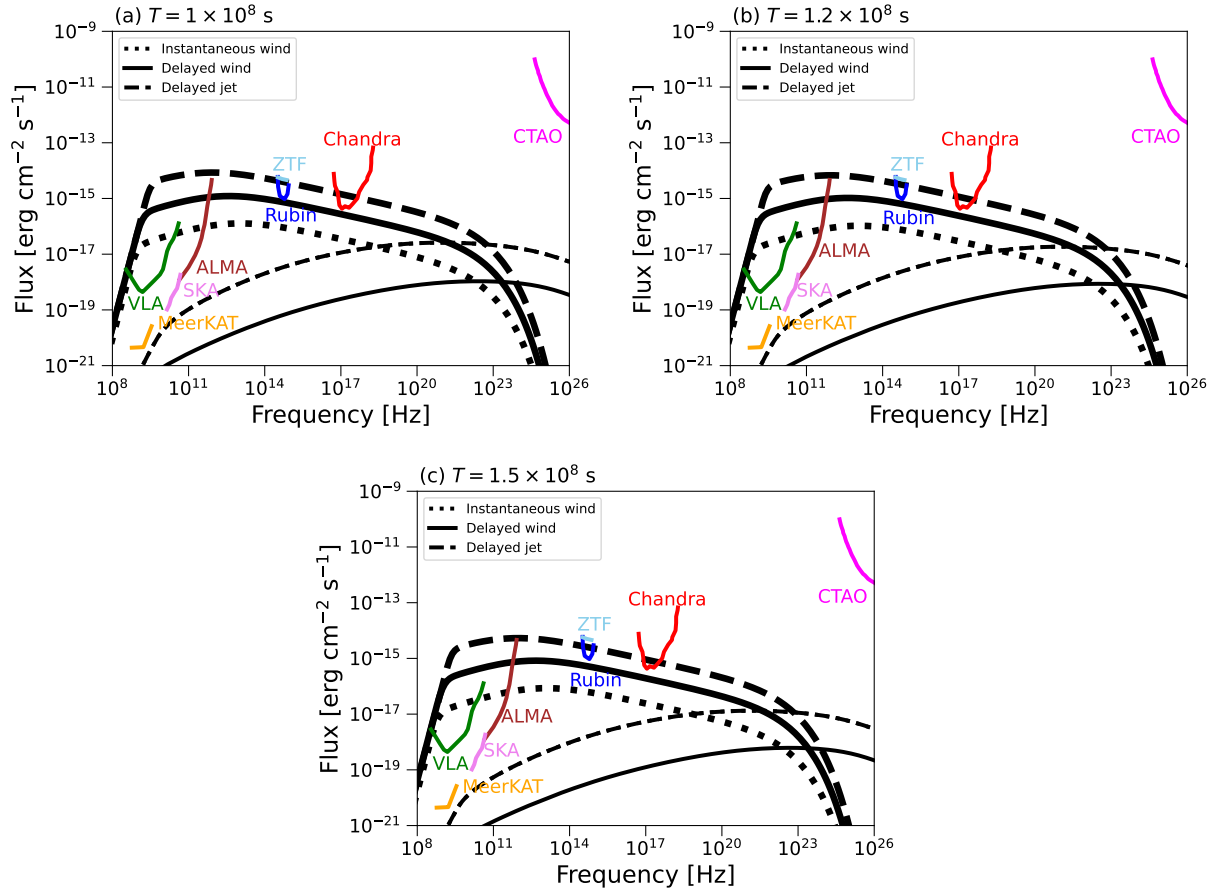


FIG. 7. Comparison of broadband nonthermal spectra from instantaneous wind, delayed wind, and delayed jet models at different epochs: 1.0×10^8 s in panel (a), 1.2×10^8 s in panel (b), and 1.5×10^8 s in panel (c). The black dotted, solid, and dashed curves correspond to the instantaneous wind, delayed wind, and delayed jet models, respectively. Synchrotron and SSC components are shown as thick and thin curves, respectively. The SSC component is calculated for all models but is negligible for the instantaneous wind model. Colored curves represent the sensitivity limits of various detectors gamma-ray (magenta: CTAO [45], 50 h), x-ray (red: Chandra [46], 100 ks), optical (blue: Rubin [47], 30 s; sky-blue: ZTF [48], 30 s), and radio (brown: ALMA [49], 1 h; violet: SKA [50], 10 h; green: VLA [51], 1 h; orange: MeerKAT [52], 1 h). A source distance of $z = 0.014$ ($d_L = 60$ Mpc) is assumed. Only the delayed jet model exceeds the x-ray and optical sensitivity limits at these epochs for a nearby TDE.

result, they consider that the CNM density transitions to a constant-density ISM at the Bondi radius, and the interaction of the outflow with this density profile is argued to play a key role in producing the observed radio flare.

A variety of physical mechanisms have been proposed to account for the delayed launching of outflows—both relativistic jets and nonrelativistic winds. One plausible scenario involves a time lag in the formation of an accretion disk, which may arise from inefficient circularization of stellar debris or from prolonged viscous timescales [29, 68, 72]. Recent multiwavelength studies suggest that such delayed accretion phases are not uncommon. Ref. [73] presented evidence that late-time radio emission—interpreted as the signature of an accretion-driven outflow—is observed in a significant fraction of optically selected TDEs, often years after the optical peak. Their analysis supports the interpretation

that some of these delayed outflows are launched either during a later super-Eddington accretion phase or possibly during a transition to a low-hard accretion state. Another plausible mechanism is the development of a disk instability at late times, which can trigger a secondary mass-ejection episode. Such instability-driven outflows have been proposed to explain delayed radio flares in several TDEs [36], and offer a natural pathway for producing a delayed wind even after the prompt circularization-driven phase has ended. A further possibility is the gradual accumulation of magnetic flux near the SMBH, enabling the eventual activation of the Blandford–Znajek process and powering of a relativistic jet [74, 75]. Furthermore, environmental factors can also influence the detectability of these outflows. For instance, a relativistic jet or wind propagating through a low-density CNM may remain radio-dark until it encounters a denser region at larger radii, thereby giving rise to delayed synchrotron

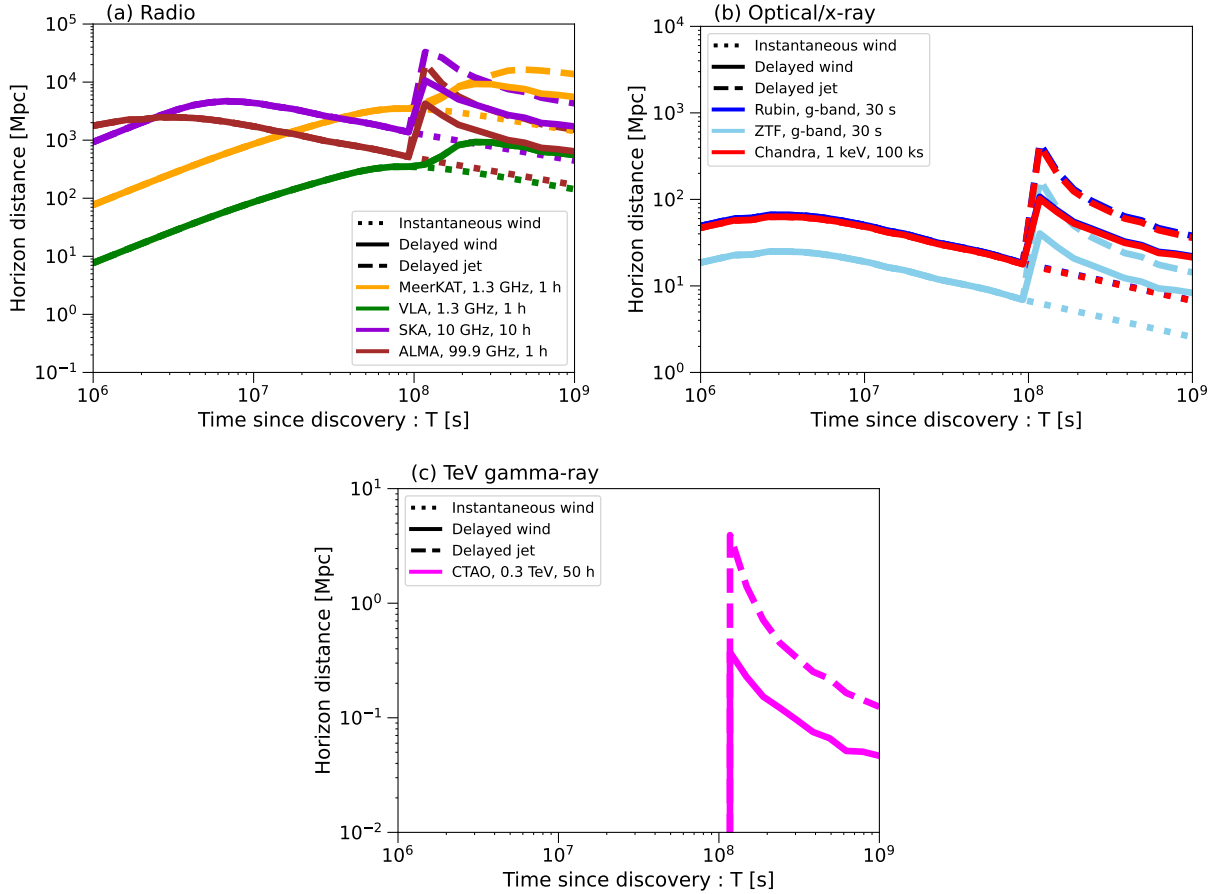


FIG. 8. Figure panels (a), (b), and (c) show the detection horizons in the radio, optical/x-ray, and TeV gamma-ray bands, respectively. The horizons for MeerKAT, VLA, SKA, ALMA, Rubin, ZTF, and Chandra are set by synchrotron emission, whereas the CTAO horizon is set by SSC emission. In the optical and x-ray bands, only the delayed jet model is detectable beyond ~ 100 Mpc, while both instantaneous wind and delayed wind models are limited to much smaller distances. The multiwavelength facilities considered here are: MeerKAT (orange, 1 h; panel a), VLA (green, 1 h; panel a), SKA (violet, 10 h; panel a), ALMA (brown, 1 h; panel a), Rubin (blue, 30 s; panel b), ZTF (sky-blue, 30 s; panel b), Chandra (red, 100 ks; panel b), and CTAO (magenta, 50 h; panel c).

emission [29, 38]. Similarly, an off-axis jet may not be detected until it slows down and the beaming cone widens, allowing for the emission to become observable along the line of sight [18, 42, 76]. Thus, the delayed observability of outflows in TDEs likely results from a combination of central engine physics—including accretion disk formation, magnetic field evolution, and state transitions—as well as CNM structure and viewing geometry.

The isotropic-equivalent kinetic energy inferred for delayed winds and delayed jets in TDEs is typically $\mathcal{E}_k^{\text{iso}} \sim 10^{52}$ erg (see Table III). For the events analyzed in this work, which are all optical TDEs, the total thermal optical radiation energy emitted from the accretion disk formed after the stellar disruption is $\sim 10^{49}$ – 10^{50} erg [77, 78]. Thus, only a small fraction of the available energy is radiated in the optical band, while the majority remains stored in the bulk kinetic motion of the outflow. This result is also consistent with previous studies [40].

In the delayed jet scenario, a relativistic outflow is

launched at $T_{\text{del}} = 10^8$ s after the stellar disruption. Our numerical calculations show that the synchrotron emission from this jet peaks around this epoch, with fluxes in both x-ray and optical bands exceeding the sensitivity limits of *Chandra* and Rubin, respectively. Notably, the optical emission remains above Rubin’s detection threshold only for a narrow time window of $\approx (1.0\text{--}1.2) \times 10^8$ s. After this, the flux declines rapidly due to jet deceleration and geometric spreading, quickly falling below the detectability threshold. With the commencement of full-scale operations at the Rubin Observatory, a substantial increase in the detection rate of optical transients is anticipated. Consequently, it is essential to establish optimal timing for follow-up observations using x-ray and radio facilities subsequent to the identification of optical emission by Rubin. Once a rising optical signal is detected around $T \sim 10^8$ s post-disruption, follow-up x-ray observations with *Chandra* should be initiated within approximately 10^6 – 10^7 s. This timescale ensures that the transient x-ray counterpart is captured before it fades be-

low the instrument's sensitivity, as the x-ray light curve in the delayed jet scenario typically peaks and declines on timescales of weeks to a few months after the jet is launched.

Although the overall delay in jet or wind launching is on the order of years ($\sim 10^8$ s), once the outflow is initiated the subsequent emission evolves on much shorter timescales ($\sim 10^6$ – 10^7 s). In particular, the rise and peak of the delayed component can develop rapidly. Therefore, high-cadence optical monitoring around $T \sim 10^8$ s is essential for discriminating between nonrelativistic winds and relativistic jets. A cadence of $\sim 10^6$ s is recommended during this critical phase to resolve the rise and peak of the delayed emission with sufficient temporal resolution. In contrast, radio emission remains detectable with ALMA, SKA, VLA, and MeerKAT throughout the evolution in all models—instantaneous wind, delayed wind, and delayed jet—owing to the lower absorption frequencies and the slower flux decay. The rise and peak of the radio light curve typically occur when the absorption frequency ν_a crosses the observing band, developing over timescales of weeks to months. To capture this evolution effectively, radio follow-up should begin promptly after the detection of late-time optical emission (within a few days), with a recommended cadence of $\sim 10^6$ s.

We comment on how T_{del} should be defined. A practical approach is to identify the onset of rebrightening in the radio light curve, which marks the interaction of a newly launched outflow with the CNM. In this case, T_{del} is inferred as the epoch when the radio flux begins to rise after an initial decline. For an initial nonrelativistic wind outflow, nonthermal optical or x-ray counterparts are not expected. A more direct constraint could be obtained if nonthermal optical or x-ray emission is detected simultaneously with the radio rebrightening, as predicted in delayed jet scenarios. In such cases, the rise of the high-energy component would provide a more accurate measurement of T_{del} . Therefore, systematic multiwavelength follow-up is essential.

We compute the detection horizons for the telescopes considered in Sec. IV using Eq. (8) of Ref. [79]. As shown in Fig. 8(b), both *Chandra* and Rubin are capable of detecting the delayed jet emission when the source is located within ≈ 400 Mpc at the time the delayed jet is launched. The optical and x-ray emission from the delayed wind model is detectable out to ≈ 100 Mpc, whereas the instantaneous wind model can be detected only within ≈ 20 Mpc due to its nonrelativistic nature and the absence of significant Doppler boosting. Rubin and ZTF operate in the same optical band, but their sensitivities are significantly different (see blue and sky-blue lines in Fig. 7), resulting in different horizon distances. The overlap between Rubin and *Chandra* reflects their similar detection horizons. Our results further indicate that CTAO can detect the TeV gamma-ray emission if the source is nearby: within $d_L \lesssim 0.4$ Mpc for the delayed wind model and $d_L \lesssim 4$ Mpc for the delayed jet model (see Fig. 8(c)). Radio facilities such as SKA and

ALMA have substantially larger detection horizons (see violet and brown lines in Fig. 8(a)). Because the delayed components become radio bright at late times, these instruments can detect the emission even if the source lies at cosmological distances up to ~ 10 Gpc at the time the delayed outflows (jet and/or wind) are launched. This implies that radio transients that brighten over several years and fade on similarly long timescales, with little or no accompanying x-ray or optical counterparts, may plausibly originate from delayed jets and/or winds associated with a TDE. Such scenarios highlight the importance of wide-field, high-sensitivity radio surveys in uncovering the otherwise hidden population of delayed TDE components.

In Sec. IV, we investigated the SSC emission. For the delayed wind and delayed jet models, two distinct outflows are present, which naturally provide two different photon fields. This raises the possibility of external inverse-Compton (EIC) scattering, in which electrons in the instantaneous wind shock upscatter photons originating from the delayed component. However, in both models, the energy density of the seed photons from the delayed component is far below the magnetic energy density in the instantaneous wind shock. Therefore, the EIC contribution is strongly suppressed. A recently detected TDE consistent with such suppressed SSC and EIC emission is AT 2025aarm [66]. Although this event occurred at a distance of ~ 60 Mpc, only upper limits have been reported in the TeV gamma-ray band [80].

In addition to the events analyzed in this work, recent observations suggest the presence of delayed outflow components in other TDEs as well [33–35]. For instance, AT 2024tvd exhibits a rapid late-time rebrightening in the radio band, which appears to require an additional delayed component to explain the observed flux evolution [34]. Similarly, WTP14adeqka does not show a clear rebrightening in the radio light curve, but its detection at very late epochs with relatively high radio luminosity also indicates the presence of a delayed outflow [35]. In both cases, however, whether the delayed component is best explained by a nonrelativistic wind or a relativistic jet remains unclear and will require detailed modeling. These recent examples highlight the growing evidence that delayed outflows may be more common in TDEs than previously expected, and reinforce the importance of systematic multiwavelength follow-up efforts to characterize their nature. On the other hand, the radio emission of AT 2018hyz also exhibits a late-time flare [28, 62]. However, its radio light curve is characterized by a rapid rise between $\sim 8 \times 10^7$ s and $\sim 2 \times 10^8$ s. Such a long-term rise in radio flux is not seen in delayed emission components, making it challenging for delayed outflow models to explain the behavior of AT2018hyz. Alternative scenarios, such as an off-axis jet model, have been proposed to account for such emission [41, 42]. AT 2018hyz may also have two jet components (see e.g., Ref. [42]).

VI. SUMMARY

In this paper, we have investigated whether radio-detected TDEs can be explained by delayed outflow models. For delayed radio flare TDEs, which exhibit radio brightening at late times, we found that emission from an instantaneous wind alone is insufficient to account for the observed light curves. This indicates that a delayed outflow, either a wind or a jet, is required to reproduce the late-time radio emission. In contrast, the TDE iPTF16fnl, which does not show a delayed radio flare, can be described by the instantaneous wind model without invoking additional components. For some delayed radio flare TDEs, both delayed wind and delayed jet models can explain the observed radio light curves. This highlights the difficulty in inferring outflow properties based solely on radio observations.

We showed that the x-ray and optical afterglow emission from delayed jets can be detected by *Chandra* and Rubin, respectively. Therefore, multiwavelength follow-up observations are essential to constrain the nature of outflows in radio-emitting TDEs and to distinguish between different emission scenarios. In particular, x-ray and optical monitoring play a critical role in identifying the properties of the radio-emitting outflows. Delayed outflows [68, 81] and underlying activities of disks and coronae [68, 82, 83] would also be important for search-

ing multimessenger signatures from TDEs.

ACKNOWLEDGEMENTS

We would like to acknowledge Kazumi Kashiyama, Asuka Kuwata, Tatsuya Matsumoto, Mainak Mukhopadhyay, Ken Ohsuga, Rin Oikawa, Shuta J. Tanaka, Seiji Toshikage, Ryo Yamazaki, and B. Theodore Zhang for useful discussions. This research was partially supported by JSPS KAKENHI, grant numbers Nos. 25KJ0010 (YS) and 20H05852 (KM). M.B. acknowledges support from the Eberly Research Fellowship at the Pennsylvania State University and the Simons Collaboration on Extreme Electrodynamics of Compact Sources (SCEECS) Postdoctoral Fellowship at the Wisconsin Ice-Cube Particle Astrophysics Center (WIPAC), University of Wisconsin-Madison. The work of K.M. is supported by the NSF Grant Nos. AST-2108466, AST-2108467 and AST-2308021. J.C. also acknowledges the Nevada Center for Astrophysics and NASA award 80NSSC23M0104 for support.

Appendix A: Adopted model parameters

In this appendix, we present the adopted model parameters. A summary of our results is provided in Table III.

- [1] J. G. Hills, Possible power source of Seyfert galaxies and QSOs, *Nature* **254**, 295 (1975).
- [2] M. J. Rees, Tidal disruption of stars by black holes of 10 to the 6th-10 to the 8th solar masses in nearby galaxies, *Nature* **333**, 523 (1988).
- [3] C. R. Evans and C. S. Kochanek, The Tidal Disruption of a Star by a Massive Black Hole, *Astrophys. J. Lett.* **346**, L13 (1989).
- [4] A. Loeb and A. Ulmer, Optical appearance of the debris of a star disrupted by a massive black hole, *Astrophys. J.* **489**, 573 (1997).
- [5] L. E. Strubbe and E. Quataert, Optical Flares from the Tidal Disruption of Stars by Massive Black Holes, *Mon. Not. Roy. Astron. Soc.* **400**, 2070 (2009).
- [6] G. Lodato and E. Rossi, Multiband lightcurves of tidal disruption events, *Mon. Not. Roy. Astron. Soc.* **410**, 359 (2011).
- [7] S. Komossa, Tidal disruption of stars by supermassive black holes: Status of observations, *JHEAp* **7**, 148 (2015).
- [8] B. D. Metzger and N. C. Stone, A bright year for tidal disruptions, *Mon. Not. Roy. Astron. Soc.* **461**, 948 (2016).
- [9] N. Roth *et al.*, The X-Ray through Optical Fluxes and Line Strengths of Tidal Disruption Events, *Astrophys. J.* **827**, 3 (2016).
- [10] K. D. Alexander *et al.*, Radio Properties of Tidal Disruption Events, *Space Sci. Rev.* **216**, 81 (2020).
- [11] F. De Colle *et al.*, The dynamics, appearance and demographics of relativistic jets triggered by tidal disruption of stars in quiescent supermassive black holes, *Astrophys. J.* **760**, 103 (2012).
- [12] S. van Velzen *et al.*, Seventeen Tidal Disruption Events from the First Half of ZTF Survey Observations: Entering a New Era of Population Studies, *Astrophys. J.* **908**, 4 (2021).
- [13] J. S. Bloom *et al.*, A relativistic jetted outburst from a massive black hole fed by a tidally disrupted star, *Science* **333**, 203 (2011).
- [14] D. N. Burrows *et al.*, Discovery of the Onset of Rapid Accretion by a Dormant Massive Black Hole, *Nature* **476**, 421 (2011).
- [15] S. B. Cenko *et al.*, Swift J2058.4+0516: Discovery of a Possible Second Relativistic Tidal Disruption Flare, *Astrophys. J.* **753**, 77 (2012).
- [16] G. C. Brown *et al.*, Swift J1112.2–8238: a candidate relativistic tidal disruption flare, *Mon. Not. Roy. Astron. Soc.* **452**, 4297 (2015).
- [17] I. Andreoni *et al.*, A very luminous jet from the disruption of a star by a massive black hole, *Nature* **612**, 430 (2022), [Erratum: Nature 613, E6 (2023)].
- [18] D. Giannios and B. D. Metzger, Radio transients from stellar tidal disruption by massive black holes, *Mon. Not. Roy. Astron. Soc.* **416**, 2102 (2011).
- [19] T. Piran *et al.*, "Circularization" vs. Accretion – What Powers Tidal Disruption Events?, *Astrophys. J.* **806**, 164 (2015).
- [20] S. van Velzen *et al.*, A radio jet from the optical and x-ray bright stellar tidal disruption flare ASASSN-14li, *Science* **351**, 62 (2016).

TABLE III. Parameters for several models are listed.

Instantaneous wind	θ_0 [rad]	v_0	$\mathcal{E}_k^{\text{iso}}$ [erg]	n_{ext} [cm $^{-3}$]	w	s	ϵ_B	ϵ_e	f_e	T_{del} [s]
ASASSN-14ae ^a				10^5	1.0	2.8	10^{-3}	0.1	0.1	
ASASSN-15oi ^{a,c}				20	1.5	2.6	8×10^{-2}	0.4	0.1	
PS16dtm ^a				10^3	1.0	2.8	10^{-2}	0.1	0.1	
iPTF16fnl ^b				20	1.0	2.8	6×10^{-2}	0.3	0.8	
ASASSN-19bt ^a	$-^d$	$0.1c$	5×10^{51}	20	1.0	2.2	4×10^{-2}	0.4	0.1	$-^e$
AT 2019dsg ^{a,c}				4×10^2	1.0	2.6	4×10^{-2}	0.3	0.1	
AT 2019ehz ^a				10^2	2.0	2.7	8×10^{-2}	0.4	0.85	
AT 2019eve ^a				5×10^2	1.0	2.2	6×10^{-2}	0.3	0.8	
AT 2020vwl ^{a,c}				10^2	1.0	2.8	3×10^{-2}	0.3	0.1	
Delayed wind	θ_0 [rad]	v_0	$\mathcal{E}_k^{\text{iso}}$ [erg]	n_{ext} [cm $^{-3}$]	w	s	ϵ_B	ϵ_e	f_e	T_{del} [s]
ASASSN-14ae ^a			5×10^{52}	10^5	1.0	2.8	10^{-3}	0.1	0.1	2.2×10^8
ASASSN-15oi ^{a,c}			5×10^{52}	20	1.5	2.1	8×10^{-2}	0.4	0.8	6.0×10^7
PS16dtm ^a			5×10^{52}	10^3	1.0	2.4	10^{-2}	0.1	0.2	4.0×10^7
iPTF16fnl ^b			5×10^{51}	20	1.0	2.8	6×10^{-2}	0.3	0.8	7.0×10^6
ASASSN-19bt ^a	$-^d$	$0.1c$	5×10^{52}	20	1.0	2.1	4×10^{-2}	0.4	0.6	10^6
AT 2019dsg ^{a,c}			5×10^{52}	4×10^2	1.0	2.6	10^{-2}	0.1	0.6	8.0×10^7
AT 2019ehz ^a			5×10^{52}	10^2	2.0	2.7	10^{-3}	0.1	0.1	10^7
AT 2019eve ^a			5×10^{52}	5×10^2	1.0	2.2	10^{-2}	0.1	0.3	10^7
AT 2020vwl ^{a,c}			5×10^{52}	10^2	1.0	2.8	2×10^{-2}	0.1	0.1	5.2×10^7
Delayed jet	θ_0 [rad]	Γ_0	$\mathcal{E}_k^{\text{iso}}$ [erg]	n_{ext} [cm $^{-3}$]	w	s	ϵ_B	ϵ_e	f_e	T_{del} [s]
ASASSN-14ae ^a				10^5	1.0	2.5	10^{-3}	10^{-3}	0.1	2.2×10^8
ASASSN-15oi ^a				20	1.5	2.1	4×10^{-3}	0.3	0.8	6.0×10^7
PS16dtm ^a				10^3	1.0	2.7	2×10^{-3}	0.1	0.1	4.0×10^7
iPTF16fnl ^b				20	1.0	2.2	3×10^{-5}	10^{-3}	0.1	7.0×10^6
ASASSN-19bt ^a	0.35	3.0	5×10^{52}	20	1.0	2.8	10^{-3}	3×10^{-2}	0.6	2.0×10^7
AT 2019dsg ^{a,c}				4×10^2	1.0	2.8	10^{-4}	0.1	0.1	8.0×10^7
AT 2019ehz ^a				10^2	1.0	2.7	3×10^{-3}	0.1	0.1	10^7
AT 2019eve ^a				5×10^2	1.0	2.6	3×10^{-3}	0.1	0.1	10^7
AT 2020vwl ^{a,c}				10^2	1.0	2.6	10^{-3}	2×10^{-2}	0.1	5.2×10^7

Notes.^a Delayed radio flare event.^b Radio event without a delayed flare.^c Rebrightening event.^d N/A (consider an isotropic outflow.)^e N/A.

[21] T. Matsumoto and T. Piran, Generalized equipartition method from an arbitrary viewing angle, *Mon. Not. Roy. Astron. Soc.* **522**, 4565 (2023).

[22] P. Beniamini, T. Piran, and T. Matsumoto, Swift J1644+57 as an off-axis Jet, *Mon. Not. Roy. Astron. Soc.* **524**, 1386 (2023).

[23] K. D. Alexander *et al.*, Discovery of an outflow from radio observations of the tidal disruption event ASASSN-14li, *Astrophys. J. Lett.* **819**, L25 (2016).

[24] T. Matsumoto, T. Piran, and J. H. Krolik, What powers the radio emission in TDE AT2019dsg: A long-lived jet or the disruption itself?, *Mon. Not. Roy. Astron. Soc.* **511**, 5085 (2022).

[25] Y. Cendes *et al.*, Radio Observations of an Ordinary Outflow from the Tidal Disruption Event AT2019dsg, *Astrophys. J.* **919**, 127 (2021).

[26] K. Hayasaki and R. Yamazaki, Disk Wind–Driven Expanding Radio-emitting Shell in Tidal Disruption Events, *Astrophys. J.* **954**, 5 (2023).

[27] A. Horesh, S. B. Cenko, and I. Arcavi, Delayed Radio Flares from a Tidal Disruption Event, *Nature Astron.* **5**, 491 (2021).

[28] Y. Cendes *et al.*, A Mildly Relativistic Outflow Launched Two Years after Disruption in Tidal Disruption Event AT2018hyz, *Astrophys. J.* **938**, 28 (2022).

[29] Y. Cendes *et al.*, Ubiquitous Late Radio Emission from Tidal Disruption Events, *arXiv e-prints* , [arXiv:2309.02275](https://arxiv.org/abs/2309.02275) (2023).

[30] C. T. Christy *et al.*, The Peculiar Radio Evolution of the Tidal Disruption Event ASASSN-19bt, *Astrophys. J.* **974**, 18 (2024), [arXiv:2404.12431](https://arxiv.org/abs/2404.12431) [astro-ph.HE].

[31] A. Horesh *et al.*, Are Delayed Radio Flares Common in Tidal Disruption Events? The Case of the TDE iPTF 16fnl, *Astrophys. J. Lett.* **920**, L5 (2021).

[32] A. J. Goodwin *et al.*, A Second Radio Flare from the Tidal Disruption Event AT2020vwl: A Delayed Outflow Ejection?, *Astrophys. J.* **981**, 122 (2025), [arXiv:2410.18665](https://arxiv.org/abs/2410.18665) [astro-ph.HE].

[33] Z. Lin *et al.*, Delayed Launch of Ultrafast Outflows in the Tidal Disruption Event AT2020afhd, *arXiv e-prints* , [arXiv:2507.15482](https://arxiv.org/abs/2507.15482) (2025).

[34] I. Sfardadi *et al.*, The First Radio-Bright Off-Nuclear TDE 2024tvd Reveals the Fastest-Evolving Double-Peaked Radio Emission, *arXiv e-prints* , [arXiv:2508.03807](https://arxiv.org/abs/2508.03807) (2025).

[35] W. W. Golay *et al.*, Radio Emission from the Infrared Tidal Disruption Event WTP14adeqka: The First Directly Resolved Delayed Outflow from a TDE, *arXiv e-prints* , [arXiv:2508.16756](https://arxiv.org/abs/2508.16756) (2025).

[36] S. C. Wu, D. Tsuna, B. Mockler, and A. L. Piro, Delayed radio emission in tidal disruption events from collisions of outflows driven by disk instabilities, *arXiv e-prints* , [arXiv:2511.14008](https://arxiv.org/abs/2511.14008) [astro-ph.HE].

[37] Z. G. Dai and T. Lu, Hydrodynamics of relativistic blast waves in a density-jump medium and their emission signature, *Astrophys. J. Lett.* **565**, L87 (2002).

[38] E. Nakar and J. Granot, Smooth Light Curves from a Bumpy Ride: Relativistic Blast Wave Encounters a Density Jump, *Mon. Not. Roy. Astron. Soc.* **380**, 1744 (2007).

[39] J. Zhuang, R.-F. Shen, G. Mou, and W. Lu, Interaction of an Outflow with Surrounding Gaseous Clouds as the Origin of Late-time Radio Flares in Tidal Disruption Events, *Astrophys. J.* **979**, 109 (2025), [arXiv:2406.08012](https://arxiv.org/abs/2406.08012) [astro-ph.HE].

[40] T. Matsumoto and T. Piran, Late-time Radio Flares in Tidal Disruption Events, *Astrophys. J.* **971**, 49 (2024), [arXiv:2404.15966](https://arxiv.org/abs/2404.15966) [astro-ph.HE].

[41] I. Sfardadi *et al.*, An off-axis relativistic jet seen in the long lasting delayed radio flare of the TDE AT 2018hyz, *Mon. Not. Roy. Astron. Soc.* **527**, 7672 (2024).

[42] Y. Sato *et al.*, Two-component off-axis jet model for radio flares of tidal disruption events, *arXiv e-prints* , [arXiv:2404.13326](https://arxiv.org/abs/2404.13326) (2024).

[43] C. Yuan, B. T. Zhang, W. Winter, and K. Murase, Structured Jet Model for Multiwavelength Observations of the Jetted Tidal Disruption Event AT 2022cmc, *Astrophys. J.* **974**, 162 (2024), [arXiv:2406.11513](https://arxiv.org/abs/2406.11513) [astro-ph.HE].

[44] C. Yuan, W. Winter, B. T. Zhang, K. Murase, and B. Zhang, Revisiting X-Ray Afterglows of Jetted Tidal Disruption Events with the External Reverse Shock, *Astrophys. J.* **982**, 196 (2025), [arXiv:2411.07925](https://arxiv.org/abs/2411.07925) [astro-ph.HE].

[45] The official website of CTAO, <https://www.ctao.org>.

[46] The official website of Chandra, <https://chandra.harvard.edu>.

[47] The official website of Rubin, <https://www.lsst.org>.

[48] The official website of ZTF, <https://www.ztf.caltech.edu>.

[49] The official website of ALMA, <https://alma-telescope.jp/en/>.

[50] The official website of SKA, <https://www.skao.int/en>.

[51] The official website of VLA, <https://public.nrao.edu/telescopes/vla/>.

[52] The official website of MeerKAT, <https://www.sarao.ac.za/science/meerkat/about-meerkat/>.

[53] B. T. Zhang *et al.*, External Inverse-Compton Emission from Low-luminosity Gamma-Ray Bursts: Application to GRB 190829A, *Astrophys. J.* **920**, 55 (2021).

[54] B. T. Zhang *et al.*, The origin of very-high-energy gamma-rays from GRB 221009A: implications for reverse shock proton synchrotron emission, *arXiv e-prints* , [arXiv:2311.13671](https://arxiv.org/abs/2311.13671) (2023).

[55] K. Murase *et al.*, On the Implications of Late Internal Dissipation for Shallow-Decay Afterglow Emission and Associated High-Energy Gamma-Ray Signals, *Astrophys. J.* **732**, 77 (2011).

[56] K. Murase, Interacting supernovae as high-energy multi-messenger transients, *Phys. Rev. D* **109**, 103020 (2024), [arXiv:2312.17239](https://arxiv.org/abs/2312.17239) [astro-ph.HE].

[57] R. A. M. J. Wijers, M. J. Rees, and P. Meszaros, Shocked by GRB-970228: The Afterglow of a cosmological fireball, *Mon. Not. Roy. Astron. Soc.* **288**, L51 (1997), [arXiv:astro-ph/9704153](https://arxiv.org/abs/astro-ph/9704153).

[58] Z. G. Dai and T. Lu, The afterglow of grb 990123 and a dense medium, *Astrophys. J. Lett.* **519**, L155 (1999), [arXiv:astro-ph/9904025](https://arxiv.org/abs/astro-ph/9904025).

[59] Y. F. Huang and K. S. Cheng, Gamma-ray bursts: Optical afterglows in the deep Newtonian phase, *Mon. Not. Roy. Astron. Soc.* **341**, 263 (2003), [arXiv:astro-ph/0301387](https://arxiv.org/abs/astro-ph/0301387).

[60] T. Piran, The physics of gamma-ray bursts, *Rev. Mod. Phys.* **76**, 1143 (2004), [arXiv:astro-ph/0405503](https://arxiv.org/abs/astro-ph/0405503).

[61] B. Zhang, *The Physics of Gamma-Ray Bursts* (2018).

[62] A. Anumarlapudi *et al.*, Radio afterglows from tidal disruption events: An unbiased sample from ASKAP RACS, *arXiv e-prints* , [arXiv:2407.12097](https://arxiv.org/abs/2407.12097) (2024).

[63] A. Hajela *et al.*, Eight Years of Light from ASASSN-15oi: Towards Understanding the Late-time Evolution of TDEs, *arXiv e-prints* , [arXiv:2407.19019](https://arxiv.org/abs/2407.19019) (2024).

[64] A. Horesh, I. Sfardadi, R. Fender, D. A. Green, D. R. A. Williams, and J. S. Bright, Are Delayed Radio Flares Common in Tidal Disruption Events? The Case of the TDE iPTF 16fnl, *Astrophys. J. Lett.* **920**, L5 (2021), [arXiv:2109.10921](https://arxiv.org/abs/2109.10921) [astro-ph.HE].

[65] A. J. Goodwin *et al.*, A radio-emitting outflow produced by the tidal disruption event AT2020vwl, *Mon. Not. Roy. Astron. Soc.* **522**, 5084 (2023).

[66] J. M. Miller and B. Mockler, Archival Swift Observations of the Host Galaxy of the TDE AT2025aarm, *The Astronomer's Telegram* **17466**, 1 (2025).

[67] J. Guillochon and E. Ramirez-Ruiz, A Dark Year for Tidal Disruption Events, *Astrophys. J.* **809**, 166 (2015), [arXiv:1501.05306](https://arxiv.org/abs/1501.05306) [astro-ph.HE].

[68] K. Murase *et al.*, High-Energy Neutrino and Gamma-Ray Emission from Tidal Disruption Events, *Astrophys. J.* **902**, 108 (2020).

[69] T. Piran, A. Sadowski, and A. Tchekhovskoy, Jet and disc luminosities in tidal disruption events, *Mon. Not. Roy. Astron. Soc.* **453**, 157 (2015), [arXiv:1501.02015](https://arxiv.org/abs/1501.02015) [astro-ph.HE].

[70] S. van Velzen *et al.*, Seventeen Tidal Disruption Events from the First Half of ZTF Survey Observations: Entering a New Era of Population Studies, *Astrophys. J.* **908**, 4 (2021), [arXiv:2001.01409](https://arxiv.org/abs/2001.01409) [astro-ph.HE].

[71] H. Bondi, On spherically symmetrical accretion, *Mon. Not. Roy. Astron. Soc.* **112**, 195 (1952).

[72] K. Hayasaki and P. G. Jonker, On the Origin of Late-time X-Ray Flares in UV/optically Selected Tidal Disruption Events, *Astrophys. J.* **921**, 20 (2021), [arXiv:2107.03666](https://arxiv.org/abs/2107.03666) [astro-ph.HE].

[73] K. D. Alexander *et al.*, The Multi-Wavelength Context of Delayed Radio Emission in TDEs: Evidence for Accretion-Driven Outflows, [arXiv e-prints](https://arxiv.org/abs/2506.12729) , [arXiv:2506.12729](https://arxiv.org/abs/2506.12729) (2025).

[74] L. Z. Kelley, A. Tchekhovskoy, and R. Narayan, Tidal Disruption and Magnetic Flux Capture: Powering a Jet from a Quiescent Black Hole, *Mon. Not. Roy. Astron. Soc.* **445**, 3919 (2014).

[75] A. Tchekhovskoy *et al.*, Swift J1644+57 gone MAD: the case for dynamically-important magnetic flux threading the black hole in a jetted tidal disruption event, *Mon. Not. Roy. Astron. Soc.* **437**, 2744 (2014).

[76] P. Mimica *et al.*, The radio afterglow of Swift J1644+57 reveals a powerful jet with fast core and slow sheath, *Mon. Not. Roy. Astron. Soc.* **450**, 2824 (2015).

[77] W. Lu and P. Kumar, On the Missing Energy Puzzle of Tidal Disruption Events, *Astrophys. J.* **865**, 128 (2018), [arXiv:1802.02151](https://arxiv.org/abs/1802.02151) [astro-ph.HE].

[78] B. D. Metzger, Cooling Envelope Model for Tidal Disruption Events, *Astrophys. J. Lett.* **937**, L12 (2022), [arXiv:2207.07136](https://arxiv.org/abs/2207.07136) [astro-ph.HE].

[79] C. Yuan, K. Murase, B. T. Zhang, S. S. Kimura, and P. Mészáros, Post-Merger Jets from Supermassive Black Hole Coalescences as Electromagnetic Counterparts of Gravitational Wave Emission, *Astrophys. J. Lett.* **911**, L15 (2021), [arXiv:2101.05788](https://arxiv.org/abs/2101.05788) [astro-ph.HE].

[80] D. Paneque, M. Teshima, M. Kherlakian, A. Simongini, H. Katagiri, F. Schiavone, S. Menon, S. Inoue, and V. B. Martins, Gamma-ray upper limits the on the rising phase of TDE 2025aarm from observations by the MAGIC and LST-1 telescopes, Transient Name Server AstroNote **328**, 1 (2025).

[81] M. Mukhopadhyay, M. Bhattacharya, and K. Murase, Multimessenger signatures of delayed choked jets in tidal disruption events, *Mon. Not. Roy. Astron. Soc.* **534**, 1528 (2024), [arXiv:2309.02275](https://arxiv.org/abs/2309.02275) [astro-ph.HE].

[82] K. Murase, S. S. Kimura, and P. Meszaros, Hidden Cores of Active Galactic Nuclei as the Origin of Medium-Energy Neutrinos: Critical Tests with the MeV Gamma-Ray Connection, *Phys. Rev. Lett.* **125**, 011101 (2020), [arXiv:1904.04226](https://arxiv.org/abs/1904.04226) [astro-ph.HE].

[83] K. Hayasaki and R. Yamazaki, Neutrino Emissions from Tidal Disruption Remnants, *Astrophys. J.* **886**, 114 (2019).